arXiv:1411.4440v1 [astro-ph.IM] 17 Nov 2014

Electric sail control mode for amplified transverse thrust

P. Toivanen, P. Janhunen, and J. Envall

Finnish Meteorological Institute, FIN-00101, Helsinki, Finland

Abstract

The electric solar wind sail produces thrust by centrifugally spanned high voltage tethers interacting with the solar wind protons. The sail attitude can be controlled and attitude maneuvers are possible by tether voltage modulation synchronous with the sail rotation. Especially, the sail can be inclined with respect to the solar wind direction to obtain transverse thrust to change the osculating orbit angular momentum. Such an inclination has to be maintained by a continual control voltage modulation. Consequently, the tether voltage available for the thrust is less than the maximum voltage provided by the power system. Using a spherical pendulum as a model for a single rotating tether, we derive analytical estimations for the control efficiency for two separate sail control modes. One is a continuous control modulation that corresponds to strictly planar tether tip motion. The other is an on-off modulation with the tether tip moving along a closed loop on a saddle surface. The novel on-off mode is introduced here to both amplify the transverse thrust and reduce the power consumption. During the rotation cycle, the maximum voltage is applied to the tether only over two thrusting arcs when most of the transverse thrust is produced. In addition to the transverse thrust, we obtain the thrusting angle and electric power consumption for the

Email address: petri.toivanen@fmi.fi ()

[1] *Telephone number*: +358-50-5471521

two control modes. It is concluded that while the thrusting angle is about half of the sail inclination for the continuous modulation it approximately equals to the inclination angle for the on-off modulation. The efficiency of the on-off mode is emphasized when power consumption is considered, and the on-off mode can be used to improve the propulsive acceleration through the reduced power system mass.

Keywords:

Electric solar wind sail, Attitude control, Transverse thrust

---

Nomenclature

A, B	=	thrusting arcs
$\mathbf{a}$	=	acceleration
a	=	power series coefficients
$\mathbf{e}$	=	unit vector
F	=	force
g	=	tether voltage modulation $\in [0, 1]$
I	=	integral
k	=	force parameter
l	=	tether length
m	=	mass
p	=	thrusting arc factor
(r, θ, ϕ)	=	spherical polar coordinates
$\mathbf{u}$	=	solar wind velocity
V	=	tether voltage
(X,Y,Z)	=	Cartesian coordinates
α	=	sail angle
κ	=	force parameter scaled to angular frequency
Λ	=	sail coning angle
μ	=	free plane tilt angle
ν	=	angular frequency
ρ	=	electric sail to centrifugal force ratio
χ	=	$\tan\alpha \tan\Lambda$
ξ	=	electric sail thrust factor
ω	=	angular velocity
$<>$	=	angular average
$<>_t$	=	temporal average

Subscripts

A, B	=	thrusting arcs
a	=	angular average
CF	=	centrifugal
ES	=	electric solar wind sail
(r, θ, ϕ)	=	spherical polar coordinates
(x, y, z)	=	Cartesian coordinates
Θ	=	thrusting arc index
0	=	reference initial value
$\perp$	=	perpendicular (radial)
$\parallel$	=	parallel (transverse)
$*$	=	orbital coordinates

Superscripts

Θ	=	thrusting arc index

1. Introduction

The thrust of the electric solar wind sail is produced through an interaction of the solar wind protons and electrostatic electric field of long electrically charged tethers [1]. The tethers are spanned centrifugally to form a sail rig slowly rotating together with the spacecraft main body (Fig. 1). The positive tether voltage of a few tens of kilovolts is actively maintained by an electron gun powered by solar panels. The spatial scale size of the electric field structure around the tethers is several hundreds of meters forming an effective sail area against the solar wind dynamic pressure. The obtained thrust is several hundreds of nN/m over the tether length [2]. The tethers are light-weight and made of micrometer thin (a few tens of μm) aluminum

wires ultrasonically bonded together [3] for redundancy against the micrometeoroid flux.

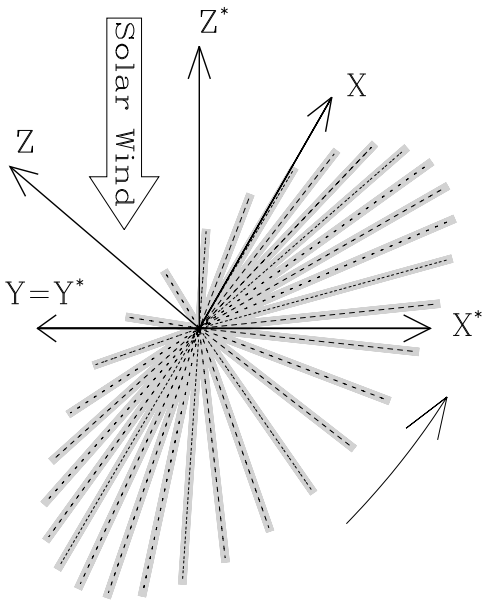

Figure 1: Slowly rotating electric solar wind sail with an electrostatic effective sail area (gray shading) around the thin tethers (dashed lines).

To maintain the tethers rotating in unison, there are two principal electric solar wind sail designs. One assumes mechanically coupled tethers by flexible auxiliary tethers connecting the main tether tips [4]. At each tether tip, there is a remote unit that includes auxiliary tether reels for the sail deployment while the main tethers are reeled out from the central body of the spacecraft. As a baseline, miniature cold gas thrusters are also included to start the sail rotation by producing the required angular momentum [5]. The other design assumes that the tethers are mechanically uncoupled and the rotation rate is controlled by freely guided photonic blades at each tether tip [6].

The electric solar wind sail attitude maintenance and maneuvers can be introduced by modulating the voltage of each tether individually and synchronously with the spacecraft rotation. The sail nominal rotation plane

can be turned to incline the sail thrust vector relative to the Sun-spacecraft direction. In the normal flying mode, the sail is inclined with respect to the Sun-spacecraft direction either to gather or diminish the osculating orbit angular momentum. In this mode, tether voltages have to be modulated continually. As the average tether voltage is less than the maximum provided by the spacecraft power system, the control mode affects the sail efficiency.

The electric solar wind sail thrusting geometry is such that the thrust generated by a single tether is along the solar wind component perpendicular to the tether (Fig. 2). For simplicity, the coordinate systems in this study are as follows. The spacecraft orbital coordinates are such that X^* is along the spacecraft orbital velocity, Z^* points to the Sun, and Y^* is normal to the orbital plane. The sail coordinates (X,Y,Z) are then rotated by the sail angle (α) around the Y^* axis as shown in Fig. 2. The thrust magnitude and direction depend then on the tether rotation phase as depicted in Fig. 2 in terms of the tether acceleration ($\mathbf{a}$). When the tether (white circle) is normal to the orbital plane (X-Z plane) the thrust has only a radial component ($\mathbf{a}_\perp$). Maximum transverse thrust ($\mathbf{a}_\parallel$) is obtained when the tether is in the orbital plane. The total thrust vector is then obtained as a rotation phase average together with the control voltage modulation combining the effects of the thrust geometry and the voltage modulation to the overall sail thrust.

Recently, the electric solar wind sail tether was modeled as a spherical pendulum [7]. As the tether is much longer (up to a few tens of kilometers) than any spacecraft spatial size, the central plate effect can be neglected, and the tether is rather a spherical than a rotating pendulum (pendulum pivot attached to a rotating plate). It was shown that there is an analytical form for the voltage modulation that maintains the sail attitude with respect to any practical Sun direction (Fig. 3). As a result, the tether rotates in a cone

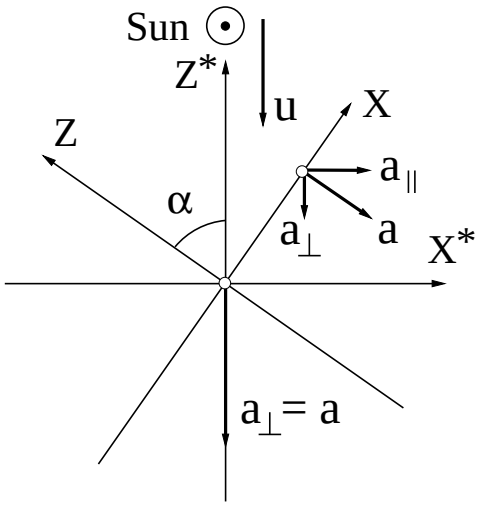

Figure 2: Geometry and rotation phase dependence of the thrust orientation in the sail coordinates (X, Z) and orbital coordinates (X^*, Z^*).

with its tip rotating in a plane. The coning angle is defined by the electric solar wind sail and centrifugal forces.

The sail guidance, including the thrust vectoring, spin plane maneuvers, attitude maintenance, and navigation in variable solar wind is a key component in mission analysis of the electric solar wind sail applications. Given the baseline of 1 N thrust of a full scale sail [8], several types of missions have been suggested and analyzed [9], [5]. These include outer solar system exploration[11], missions in non-Keplerian orbits[10], asteroid missions[12],[13], and protection from hazardous asteroids[13],[14]. Many of these missions require accurate navigation to the target in variable solar wind conditions[15]. Based on the results of this paper, the thrust vectoring and sail control mode efficiency in terms of the transverse thrust and electric power consumption are available for the future sail navigation and mission analysis.

In this paper, the motion of an on-off controlled tether is analyzed in

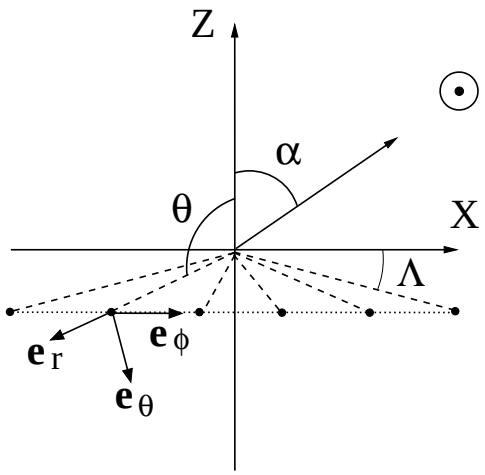

Figure 3: Number of tethers (dashed lines) in the sail coordinates with their attitude defined by the sail (α) coning (Λ) angles, and the spherical coordinate unit vectors ($\mathbf{e}_r, \mathbf{e}_\theta, \mathbf{e}_\phi$).

Section 2. The efficiencies of the smooth and on-off and control modes are obtained in Section 3. The control modes are then compared in Section 4 in terms of the transverse thrust, electric power consumption, and thrusting angle.

2. Analysis of tether motion for on-off mode

2.1. Equations of motion

The tether dynamics with a fixed tether length can be described as a spherical pendulum with equations of motion

$$a_\theta = \ddot{\Lambda} + \cos\Lambda \sin\Lambda\, \dot{\phi}^2 = -gk\,(\sin\alpha \sin\Lambda \cos\phi + \cos\alpha \cos\Lambda) \quad (1)$$

$$a_\phi = \cos\Lambda \ddot{\phi} - 2\sin\Lambda \dot{\Lambda}\dot{\phi} = -gk \sin\alpha \sin\phi. \quad (2)$$

The acceleration (a_θ, a_ϕ) is given in spherical coordinates (r, θ, ϕ) corresponding to the sail coordinates as defined in Figs. 2 and 3. The equations of motion are given in terms of the coning angle $\Lambda = \theta - \pi/2$. Assuming that the

tether has a constant linear mass density, the tether motion is parametrized by

$$k = \frac{3\xi u}{2m}, \tag{3}$$

where ξ is constant arising from the electric sail thrust law [2], u is the solar wind velocity, and m is the tether mass. Note that k is negative as the nominal solar wind (u) is flowing antiparallel with Z^* axis. The tether voltage modulation is given by $g \in [0, 1]$.

Our aim is to seek a piecewise solution for the equation of motion as sketched in Fig. 4. The solution consists of two sections of free planar motion ($g = 0$, solid curve) connected by two thrusting arcs ($g = 1$, thick solid curve). The solution is given as $\Lambda(\phi)$ and $\dot{\phi}(\phi)$ separately for the free motion and the forced thrusting motion. The forced motion is solved as a power expansion in ϕ, and its free parameters are fixed by the continuity conditions at the limits of thrusting arcs.

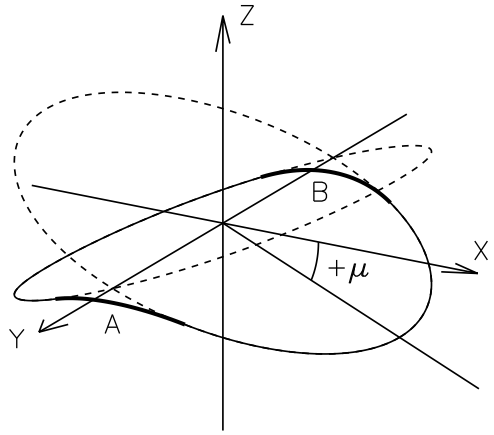

Figure 4: Tether tip trajectory (solid curve) in sail coordinates for on-off control mode. Two thrusting arcs A and B ($g = 1$, thick solid curve) connects the free planar motion ($g = 0$) on two planes (dashed lines) inclined by $\pm\mu$.

2.2. Free tether motion

When the tether voltage is off ($g = 0$), the tether rotates in a plane with angular speed ω with

$$\omega^2 = \cos^2\Lambda\dot{\phi}^2 + \dot{\Lambda}^2. \tag{4}$$

The angular speed is a constant of free motion. The equation of the plane can be given as

$$\tan\Lambda + \tan\mu\sin\phi = 0, \tag{5}$$

where we have assumed that the plane is tilted around Y axis by angle μ as shown in Fig. 4. Furthermore, Eq. (2) can be written as

$$\frac{\mathrm{d}}{\mathrm{dt}}(\cos^2\Lambda\dot{\phi}) = 0. \tag{6}$$

implying that the Z component of the angular velocity is a constant of motion. The free motion is fixed ($\omega \equiv \omega_0$) at $(X, Y, Z) = (0, l\cos\mu, l\sin\mu)$, where $\phi = \pi/2$, $\Lambda =\mid \mu \mid$, and $\dot{\Lambda} = 0$. Using Eq. (4) at this point, the constant associated with Eq. (6) can be fixed, and $\cos^2\Lambda\dot{\phi} = \omega_0\cos\mu$. Finally, solving $\cos^2\Lambda$ using Eq. (5), the square of the angular frequency can be written as

$$\dot{\phi}^2 = \frac{\omega_0^2(1+\tan^2\mu\sin^2\phi)^2}{1+\tan^2\mu}. \tag{7}$$

2.3. Forced tether motion

When the voltage is turned on the tether leaves the initial plane of free motion and adopts another plane when the voltage is turned off again. Especially, one can first consider two planar tether tip orbits as shown with dashed curves in Fig. 4. When the tether voltage is turned on for the sector (thrusting arc A) near the positive X axis, the tether tip transits from one plane to the other ($\mu \to -\mu$). Turning the voltage on around negative X axis (arc B), the tether returns to the initial plane. In Appendix A, we show that such trajectories exist. For given arc length A (ϕ_A), electric solar wind

sail force parameter (k), and tether initial angular speed (ω_0), the free plane tilt angle

$$\tan\mu = \kappa_0 \cos\alpha\phi_A(1 - 2\kappa_0 \sin\alpha\phi_A^2 + \mathcal{O}(\phi^4)), \tag{8}$$

and arc length B

$$\phi_B = \phi_A(1 - 4\kappa_0 \sin\alpha\phi_A^2 + \mathcal{O}(\phi^4)) \tag{9}$$

can be solved to define the tether motion under the on-off modulation. Note that the arcs are nonsymmetric due to the sail inclination, and $\kappa_0 = k/\omega_0^2$.

Fig. 5 shows the tether local coning angle and angular velocity as functions of azimuthal angle ϕ. The largest descent of the tether from X-Y plane is at Y axis corresponding to free plane inclination μ. The closest approaches are at X axis as determined by Λ_A and Λ_B in Eq. (A.17). The asymmetry in thrusting arcs A and B is due to the sail angle being 45°. The asymmetry is also reflected in the minimum and maximum angular velocities as given by ν_A and ν_B in Eq. (A.16). The analytical solutions are well justified against the numerical solution for the thrusting arcs A and B as shown by the dashed curves. Note that the deviation of the analytical solution from the numerical one is mostly due to the fact that the thrusting arc half length ϕ_A being 45° is pushing the limits of the approximation based on a power series expansion in ϕ.

3. Analysis of control mode efficiencies

The Cartesian components of the acceleration in terms of the spherical components read as

$$a_x = -a_\theta \sin\Lambda \cos\phi - a_\phi \sin\phi \tag{10}$$

$$a_y = -a_\theta \sin\Lambda \sin\phi + a_\phi \cos\phi \tag{11}$$

$$a_z = -a_\theta \cos\Lambda \tag{12}$$

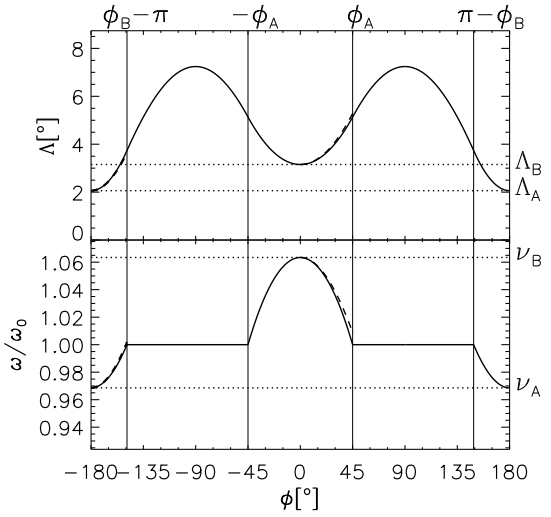

Figure 5: Analytical (solid) and numerical (dashed) solutions for the tether coning angle Λ (upper panel) and angular velocity (lower panel) as functions of azimuthal angle ϕ with $\alpha = 45°$.

that are given in terms of the coning angle Λ as in Eq. (1) and Eq. (2). The acceleration is calculated in the sail coordinates and must be rotated by the sail angle to the orbital coordinates for the radial and transverse thrust components.

To compare the control mode efficiencies, it is assumed that the tether is initially rotating freely with $\omega = \omega_0$ before any control mode is applied. Then we define a parameter ρ as a ratio of the electric solar wind sail ($F_{ES} = \xi \mid u \mid l$) and the centrifugal force ($F_{CF} = 1/2 m\omega_0^2 l$) integrated over the tether length l,

$$\rho = \frac{F_{ES}}{F_{CF}} = \frac{2\xi \mid u \mid}{m\omega_0^2} = \frac{4}{3}\frac{\mid k \mid}{\omega_0^2}. \tag{13}$$

Use of ρ is motivated by the fact that the coning angle (λ) is not a natural parameter for the on-off mode tether attitude ($\dot{\lambda} \neq 0$) as it is for the smooth mode ($\dot{\lambda} = 0$).

The electric power for the electric solar wind sail tether depends on the

tether voltage V and is proportional to $V^{3/2}$ [16]. Thus the power estimate is then proportional to the temporal average of $g^{3/2}$ over the rotation period ($< g^{3/2} >_t$). For simplicity, however, we consider the angular average $< g >^{3/2}$ as the power estimate. Numerical calculations show that this simplification underestimates the power consumption of the smooth mode by a few percent ($< 4\%$) depending on the sail plane inclination and the ratio of sail and centrifugal forces.

3.1. Smooth mode efficiency

Using the equation of motion, it can be shown that modulation

$$g = \left(\frac{1-\chi}{1+\chi\cos\phi} \right)^3 \tag{14}$$

keeps the sail coning angle constant [7], where $\chi = \tan\alpha \tan\Lambda$. Note also that the control signal is normalized to its maximum value ($\max(g) = 1$) instead of $< g >= 1$ [7].

When the smooth modulation is turned on the tether proceeds to rotate with some coning angle Λ. During a slow transition, Eq. (6) holds, ω_Z is an adiabatic invariant, and

$$\nu_a \cos^2\Lambda = \omega_0, \tag{15}$$

where ν_a is the angular average of the angular frequency ($< \dot{\phi} >$). Furthermore, substituting Eq. (14) in Eq. (1), averaging over the rotation phase ($\ddot{\Lambda} = 0$), and using Eqs. (13) and (15), we write

$$\rho = \frac{4\sin\Lambda}{3\cos\alpha\cos^4\Lambda} \frac{(1-\chi^2)^{\frac{3}{2}}}{(1-\chi)^3} \tag{16}$$

in terms of the coning angle Λ ($\chi = \tan\alpha\tan\Lambda$). The integral associated with the averaging is given by Eq. (B.1) of Appendix B. The coning angle Λ can then be solved numerically as a function of ρ as shown in Fig. 6.

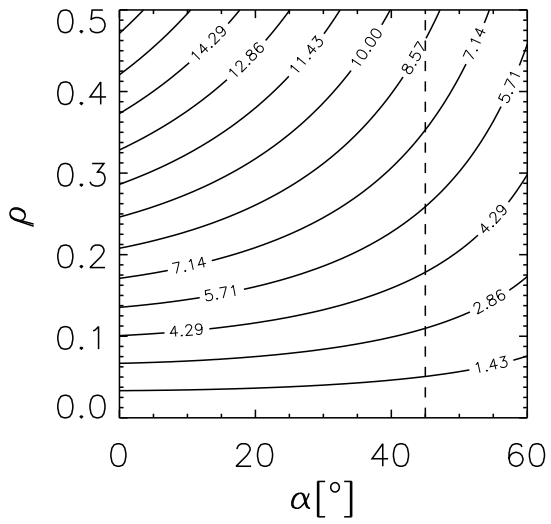

Figure 6: Coning angle for smooth modulation

To calculate the thrust, the spherical components of the acceleration of Eqs. (1) and (2) are replaced by Eqs. (10)–(12). Non-zero components of the rotation phase averaged acceleration components can be written as

$$\begin{aligned} < a_x > &= k(\sin\alpha < g > + \cos\alpha\cos\Lambda\sin\Lambda < g\cos\phi > \\ &- \sin\alpha\cos^2\Lambda < g\cos^2\phi >) \qquad (17) \\ < a_z > &= k\cos\alpha\cos^2\Lambda\,(< g > +\chi < g\cos\phi >). \qquad (18) \end{aligned}$$

after using trigonometric identities.

The phase averaged quantities are of the form of $< g\cos^n\phi >= (1-\chi)^3 I_n$ where

$$I_n = \frac{1}{2\pi}\int_0^{2\pi} \frac{\cos^n\phi d\phi}{(1+\chi\cos\phi)^3}, \;\; n = 0, 1, 2. \qquad (19)$$

These integrals can be executed by a computer algebra system such as Maxima[17] and are given in Appendix B. The average modulation $< g >$ needed for the power consumption estimate reads as

$$< g >= (1-\chi)^3 I_0 = \frac{(1-\chi)^3(2+\chi^2)}{2(1-\chi^2)^{\frac{5}{2}}}. \qquad (20)$$

After some manipulation, the phase averaged acceleration components read as

$$< a_x > = \frac{k}{2} \sin\alpha \cos 2\Lambda \, \frac{(1-\chi)^3}{(1-\chi^2)^{\frac{3}{2}}} \tag{21}$$

$$< a_z > = k \cos\alpha \cos^2\Lambda \, \frac{(1-\chi)^3}{(1-\chi^2)^{\frac{3}{2}}}. \tag{22}$$

The Y component of the acceleration includes terms proportional either to $< g \sin\phi >$ or $< g \sin\phi \cos\phi >$ that equal to zero. Finally, these components are rotated to the orbital coordinates giving the radial and transverse thrust as

$$a_\perp = \frac{k}{2} \frac{(1-\chi)^3}{(1-\chi^2)^{\frac{3}{2}}} (2\cos^2\Lambda - \sin^2\alpha) \tag{23}$$

$$a_\parallel = -\frac{k}{4} \frac{(1-\chi)^3}{(1-\chi^2)^{\frac{3}{2}}} \sin 2\alpha \tag{24}$$

The thrust angle can be expressed by

$$\tan\psi = \frac{a_\parallel}{a_\perp} = -\frac{\sin 2\alpha}{2(\cos^2\Lambda - \sin^2\alpha)}. \tag{25}$$

3.2. On-off mode efficiency

For the on-off mode, the tether attitude can be described by the tilt angle of the free plane (μ) as a function of ρ and α (Fig. 7). This corresponds to the the maximum instantaneous tether coning angle and is about half of the smooth mode coning angle shown in Fig. 6.

The efficiency analysis of the on-off mode can be carried out by using the results of Section 2.3. The average modulation for the power consumption can be written as

$$< g >= \frac{1}{\pi}(2\phi_A + \delta\phi) \approx \frac{2}{\pi}\phi_A(1 - 2\kappa_0 \sin\alpha\phi_A^2 + \mathcal{O}(\phi_A^4)). \tag{26}$$

Similarly to the smooth mode efficiency analysis, using Eqs. (1), (2), (10), (11), (12), and linearizing in Λ, the averaged components of acceleration can

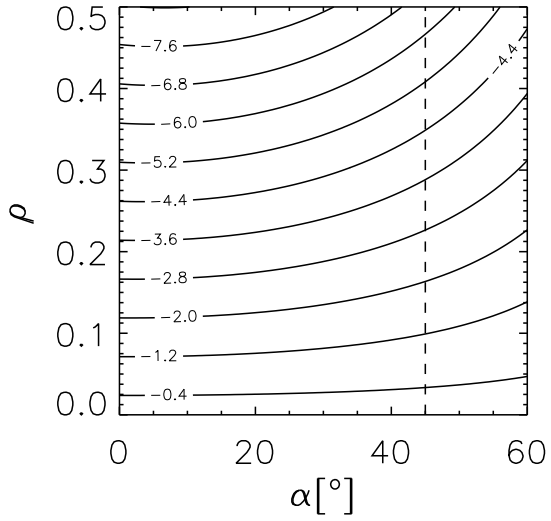

Figure 7: Isocontours of free plane tilt angle in degrees for $\phi_A = 22.5°$.

be written as

$$< a_x > = k(\cos\alpha < g\Lambda\cos\phi > + \sin\alpha < g\sin^2\alpha >) \quad (27)$$

$$< a_z > = k(\sin\alpha < g\Lambda\cos\phi > + \cos\alpha). \quad (28)$$

Expanding these components in ϕ, integrating over the arcs A and B, and rotating the acceleration components to the orbital coordinates, the average radial and transverse components of the acceleration can be written as

$$\begin{aligned} a_\perp &= \frac{2k}{\pi}\phi_A(\cos^2\alpha \\ &+ 1/3\,(\sin^2\alpha - 10\kappa_0\sin\alpha\cos^2\alpha)\phi_A^2 + \mathcal{O}(\phi_A^4)) \quad (29) \\ a_\parallel &= -\frac{k}{\pi}\phi_A(\sin 2\alpha \\ &- 1/3\,(\sin 2\alpha - 4\kappa_0\cos^3\alpha(1 - 4\tan^2\alpha))\phi_A^2 + \mathcal{O}(\phi_A^4)) \quad (30) \end{aligned}$$

The thrusting angle of the on-off modulation can be expressed then as

$$\begin{aligned} \tan\psi &= -\tan\alpha \\ &+ 1/3\,(1 + \tan^2\alpha)(\tan\alpha - 2\kappa_0\cos\alpha)\phi_A^2 + \mathcal{O}(\phi_A^4), \quad (31) \end{aligned}$$

where the leading term is $-\tan\alpha$ as expected. The minus sign is due to the definition of $a_\perp$ being negative for all sail angles.

4. Results: control mode comparison

4.1. Power consumption

The estimates for the power consumption of the control modes were given by Eq. (20) and Eq. (26). Fig. 8 shows power consumption for the smooth modulation. It can be seen that the control mode efficiency falls considerably as a function of ρ and sail angle. For the on-off modulation, the power consumption is about 0.12-0.15 times of the maximum of the smooth modulation as shown in Fig. 9. Note that this depends on the thrusting arc length. Weak dependence on ρ and sail angle arises from the fact that for non-zero sail angle the thrusting arcs are different in length according to Eq. (A.21).

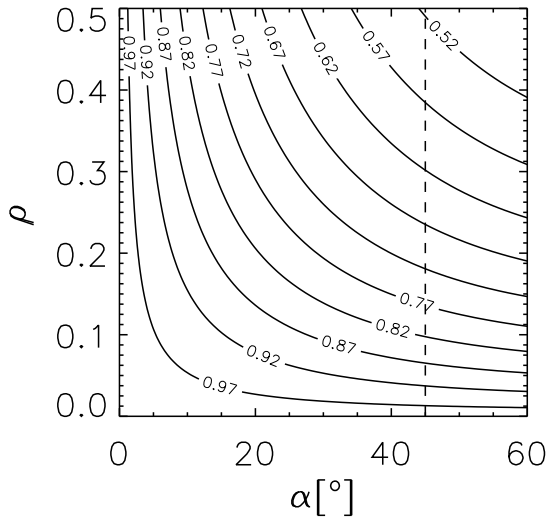

Figure 8: Power consumption of smooth modulation.

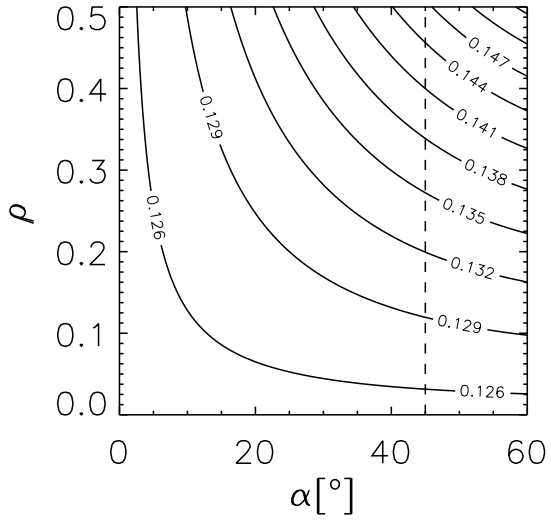

Figure 9: Power consumption of on-off modulation with $\phi_A = 22.5°$.

4.2. Transverse thrust

Another important parameter to characterize the control modes is the amount of transverse thrust. Figs. 10 and 11 show the transverse thrust for smooth and on-off modulations as obtained from Eq. (24) and Eq. (30), respectively. The transverse thrust is scaled to the maximum total thrust (1) obtained for the smooth modulation with fast rotating sail and zero sail angle (ρ, α) = (0,0). It can be seen that the transverse thrust is about 25% of the total thrust for the smooth modulation. In addition, the transverse thrust falls significantly both in α and ρ from its maximum. For example, the transverse thrust is about 17% when $\rho \approx 3.5$, corresponding to a coning angle of 7°. Note that the same behavior can be obtained by the sail angle of about 20° for a fast spinning sail (zero coning angle). These results indicates that the stronger the tether material is, the smaller fraction of available power is required for the sail attitude control, and the more efficient the sail is.

For the on-off modulation, the transverse thrust is about 10% for properly inclined sail. Note that it is expected that the transverse thrust of the on-off

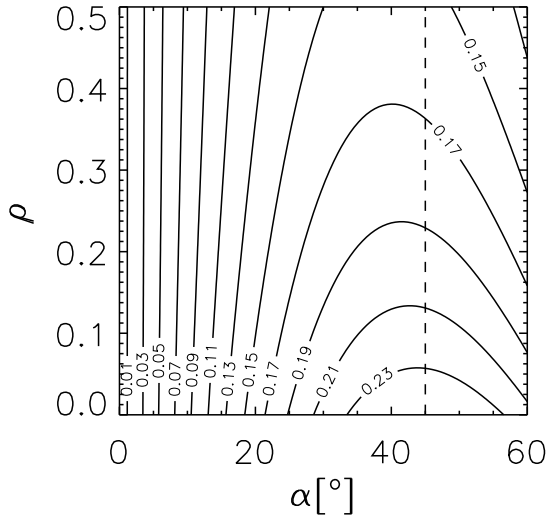

Figure 10: Transverse thrust for smooth modulation scaled to the maximum total thrust.

modulation is smaller than that given by smooth modulation since a fraction of the transverse thrust comes outside the thrusting arc. Another way to compare the transverse thrust is to scale the control mode transverse thrust by the power system mass that is proportional to the power consumption. The scaling factor is about 0.15 as the maximum of the power consumption of the on-off mode shown in Fig. 11. Thus the maximum scaled transverse thrust is about 0.8 (= 0.12/0.15) to be compared with 0.23 of the smooth mode (Fig. 11).

4.3. Thrust angle

To compare the radial and transverse thrust for the control modes, Figs. 12 and 13 show the thrust angle. In the case of the smooth modulation, the thrust angle is about half of the sail angle and reaches its maximum (about 20°) when the sail angle of 45°. There is no use of turning the sail more than 45° in terms of the thrust angle when using the smooth modulation. For the on-off modulation, the thrust angle roughly equals to the sail angle.

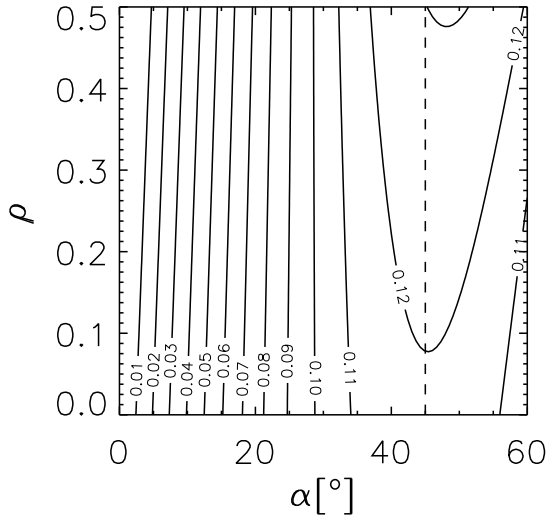

Figure 11: Transverse thrust for on-off modulation

5. Discussion

In this work, we assumed that the tether dynamics can be described by a spherical rigid rod pendulum. The single pendulum that is mechanically uncoupled to the neighboring tethers describes the electric solar wind sail design assuming freely guided photonic blades for the additional spin rate control. The ultimate difference in tether dynamics of this design is that the tether rotation rate varies in rotation phase, especially when the smooth modulation is used. This implies a voltage modulation amplitude larger than that required for the mechanically coupled design. Thus the smooth mode efficiency is underestimated in this study for the auxiliary tether design with the tethers rotating in unison. In the case of the on-off modulation, the tether rotation rate variation is negligible, and it can be expected that the estimates given here are valid for the auxiliary tether design when using the on-off modulation. For better analytical estimates for the smooth modulation, the electric solar wind sail can be assumed as a rigid body with a number of tethers connected by the auxiliary tethers as a future study.

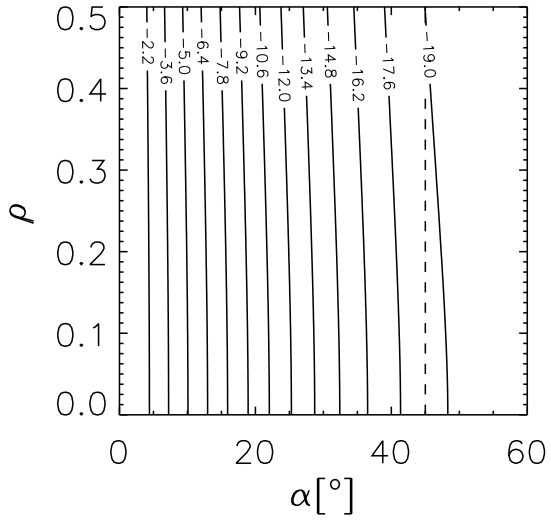

Figure 12: Thrust angle for smooth modulation

In practice, realistic tether voltage finite rise and decay times have to be taken into account. This affects both the tether control and the efficiency estimates. We tested a simple control routine to see that the tether tip can be maintained on a closed loop resembling closely the motion of the on-off modulated tether described here. The scheme was such that the sail coordinates were rotated back (and forth) corresponding to the flip of the free rotation plane while the tether was moving along arcs A (and B). In these rotated coordinates, we controlled the temporal change of the tether local coning angle to keep the tether rotating in (X,Y) plane of the rotated coordinates system. The scheme resulted in a smoothed on-off tether modulation signal. As the scheme is far from being technically feasible for the tether control as such the result were not discussed in detailed in this paper. We anticipate however that the efficiency estimates do not change dramatically due to the on-off modulation with realistic rise and decay times.

In reality, the tethers are flexible and the sail cannot be rotated infinitely fast the tethers to behave as rigid rods under the centrifugal force. Thus it

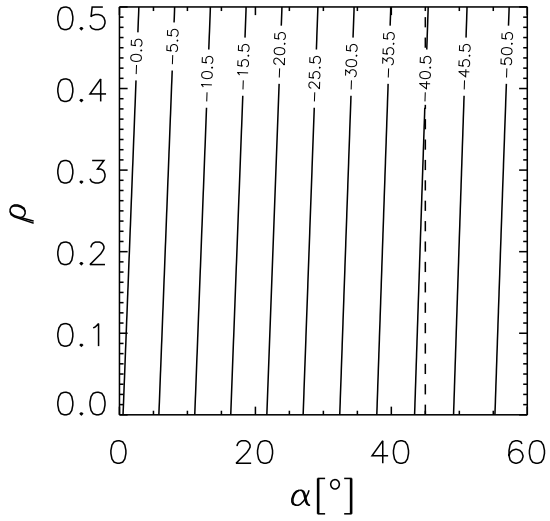

Figure 13: Thrust angle for on-off modulation

can be expected that the on-off modulation may cause some undesired slow oscillations of the tether, especially if the rotation frequency meets the tether oscillation eigenmode frequency. This issue has to be addressed by a fully dynamical simulation with a flexible tether. At this stage, it can be argued that these frequency ranges can be designed not be in resonance with each other. Furthermore, the realistic tether voltage rise and decay times smooths out transients that may be causes for harmful tether oscillations.

The real flexible tethers also implies that the local coning angle decreases towards the tip of the rotating tether due to the enhancing centrifugal force along the tether. The effective coning angle of a flexible tether is then less than that obtained from the ratio of the electric sail and the centrifugal forces for a rigid rod, and the results here underestimate the efficiency of the smooth control mode. However, solving the actual shape and effective coning angle of the flexible tether as a future study, the results shown here are applicable by replacing the coning angle used with the effective coning angle.

6. Conclusions

Two electric solar wind sail attitude control schemes were analyzed in this paper. One assumes smooth tether voltage modulation consistent with strictly planar tether tip motion. The other is based on an on-off voltage modulation leading to a non-planar but closed loop tether tip motion. The tether motion of the former mode is based on earlier results while the solution for the tether tip motion of the latter mode was derived here in details. Having the dynamics of the both modes solved, the efficiency of the control modes was addressed in terms of the sail transverse thrust, thrust angle, and power consumption. The primary findings are summarized below.

The analysis of the on-off modulation showed that the tether tip draws a closed loop on a surface that is a combination of two planes and a saddle surface. The tether tip moves along planar orbits when the tether voltage is off (free motion) and transits from one plane to the other on the saddle surface when the voltage is on (forced motion, thrusting arc). The motion was solved as a function of given length of the trusting arc, sail angle with respect to the Sun direction, and ratio of the electric solar wind sail thrust to the centrifugal force.

The transverse thrust efficiency of the smooth modulation combines two effects. One is the electric sail force geometry and the other is the tether voltage modulation. The thrust is proportional to the solar wind component perpendicular to the tether. Thus the instantaneous thrust direction changes from being fully radial (tether normal to the orbital plane) to having both radial and transverse components defined by the sail angle (tether in orbital plane). The crest-to-trough ratio of the voltage modulation increases with increasing tether coning angle. The thrust averaged over the rotation phase leads then to an efficiency that decreases strongly depending on the coning

angle. For a coning angle close to 0° (7°), the transverse thrust is about 0.23 (0.17) times the total thrust at the sail angle of 45°. This means that a fast spinning sail is more efficient implying the importance of the tether material tensile strength for the sail efficiency.

The on-off modulation was motivated by the fact that the transverse thrust is mostly produced in relatively narrow sectors around the orbital plane. Having the tether voltage fully on only along these thrusting arcs, most of the transverse thrust is captured. Having the voltage off elsewhere reduces the radial thrust. As the result, the transverse thrust generated is about 0.12 times the total thrust available in a wide range of the sail angle and electric sail force to centrifugal force ratio (ρ). Thus, for realistic ρ values, it approaches the smooth mode efficiency values. Furthermore, the power consumption is 0.13 times the smooth modulation consumption. Thus the transverse thrust efficiency scaled to the power system mass (proportional to power consumption) is about 0.8 for the on-off mode and 0.23 for the smooth mode. Finally, the thrust angle of the on-off mode approximately equals the sail angle. For the smooth mode, the thrust angle is about half of the sail angle with the maximum of about 20° reached at 45° after which the thrust angle is constant for sail angles less than 60°. The numbers given here are for a thrusting arc length of 45°.

Appendix A.

The equation of motion Eqs. (1)–(2) can be solved for the on-off modulation as follows. The orbital change associated with the flip of the free plane takes place near the plane of $Z = 0$ for arcs A and B (Fig. 4) where the coning angle $\Lambda \approx 0$. Thus the equation of motion Eqs. (1)–(2) can be linearized in Λ around both $\phi \approx 0$ and $\phi \approx \pi$. The equation of motion can

then be written as

$$\ddot{\Lambda} + \Lambda\dot{\phi}^2 = -k\,(p\Lambda \sin\alpha\cos\phi + \cos\alpha) \tag{A.1}$$

$$\ddot{\phi} = -pk\sin\alpha\sin\phi, \tag{A.2}$$

where we have added factor $p = \pm 1$ to include both arcs A ($p = 1$) and B ($p = -1$) in the analysis while further expansions in ϕ can be considered at $\phi = 0$ for both arcs. Similarly, the plane of free motion of Eq. (5) is linearized to read as

$$\Lambda + \tan\mu\sin\phi = 0 \tag{A.3}$$

for both arcs since for the arc B, the flipping of the plane of the free rotation ($\mu \to -\mu$) and expansion around $\phi \approx \pi$ ($\sin(\phi + \pi) = -\sin\phi$) cancels.

Next, Eq. (A.2) can be solved to read as

$$\dot{\phi}^2 = \nu_\Theta^2 + 2pk\sin\alpha(\cos\phi - 1), \tag{A.4}$$

where the constant of integration (ν_Θ^2) is such that the angular frequency equals to ν_Θ at $\phi = 0$. The subscript Θ denotes the tether thrusting arc A or B. Using the chain rule ($\ddot{\Lambda} = (d^2\Lambda/d\phi)\dot{\phi}^2 + (d\Lambda/d\phi)\ddot{\phi}$) in Eq. (A.1) and replacing both $\dot{\phi}^2$ and $\ddot{\phi}$ with Eq. (A.4) and Eq. (A.2), respectively, differential equation for $\Lambda(\phi)$ can be written as

$$\begin{aligned} & \frac{d^2\Lambda}{d\phi^2}[1 + 2p\kappa_\Theta\sin\alpha(\cos\phi - 1)] - \frac{d\Lambda}{d\phi}p\kappa_\Theta\sin\alpha\sin\phi \\ + \quad & \Lambda[1 + p\kappa_\Theta\sin\alpha(3\cos\phi - 2) + p\kappa_\Theta\sin\alpha] + \kappa_\Theta\cos\alpha = 0, \end{aligned} \tag{A.5}$$

where $\kappa_\Theta = k/\nu_\Theta^2$.

As a next step, we replace $\sin\phi$ and $\cos\phi$ by their power expansions in Eqs. (A.4) and (A.5). First, $\dot{\phi}^2$ can be readily written as

$$\dot{\phi}^2 \approx \nu_\Theta^2 - pk\sin\alpha\phi^2 + \mathcal{O}(\phi^4). \tag{A.6}$$

Then $\Lambda(\phi)$ can be solved as a power series as

$$\Lambda = \sum_{i=0}^{N} a_i \phi^i. \tag{A.7}$$

The coefficients a_i can be obtained by a computer algebra systems such as Maxima [17], and $\Lambda(\phi)$ can be written as

$$\Lambda \approx \Lambda_\Theta + a_2^\Theta \phi^2 + \mathcal{O}(\phi^4), \tag{A.8}$$

where

$$a_2^\Theta = -\frac{1}{2}\left(\Lambda_\Theta(1 + 2p\kappa_\Theta \sin\alpha) + \kappa_\Theta \cos\alpha\right) \tag{A.9}$$

and is given in terms of the free coefficient $a_0^\Theta = \Lambda_\Theta$ to be determined by the continuity conditions at $\phi = \pm\phi_\Theta$. As it can be expected, $\Lambda(\phi)$ is symmetric as

$$a_3^\Theta = -\frac{1}{6} a_1^\Theta (1 + p\kappa_\Theta \sin\alpha) = 0 \tag{A.10}$$

since $a_1^\Theta = \dot{\Lambda}_\Theta = 0$ when $\phi = 0$. For the free motion, $\lambda(\phi)$ in Eq. (A.3) and $\dot{\phi}$) in Eq. (7) read as

$$\Lambda \approx -\tan\mu(\phi - 1/6\,\phi^3 + \mathcal{O}(\phi^5)) \tag{A.11}$$

and

$$\dot{\phi}^2 \approx \frac{\omega_0^2}{1 + \tan^2\mu}(1 + 2\tan^2\mu\phi^2 + \mathcal{O}(\phi^4)) \approx \omega_0^2 \tag{A.12}$$

as expanded in ϕ. In Eq. (A.12), $\dot{\phi}^2 \approx \omega_0^2$ when only the linear terms in $\tan\mu$ are considered.

To solve $\Lambda_\Theta, \nu_\Theta, \tan\mu$, and ϕ_B in terms of the free parameter ϕ_A the continuity equations for Λ, $\dot{\Lambda}$ and $\dot{\phi}^2$ are written. As $\Lambda(\phi)$ and $\dot{\phi}(\phi)$ are symmetric at origin, these equations read as

$$\Lambda_\Theta + a_2^\Theta \phi_\Theta^2 = -\tan\mu(\phi_\Theta - 1/6\,\phi_\Theta^3) \tag{A.13}$$

$$2a_2^\Theta \phi_\Theta = -\tan\mu(1 - 1/2\,\phi_\Theta^2) \tag{A.14}$$

$$\nu_\Theta^2 - pk\sin\alpha\phi_\Theta^2 = \omega_0^2. \tag{A.15}$$

For both arcs A and B, ν_Θ^2 and Λ_Θ can be solved in terms of $\tan\mu$ and ϕ_Θ as

$$\nu_\Theta^2 = \omega_0^2 + pk\sin\alpha\phi_\Theta^2 \tag{A.16}$$

and

$$\Lambda_\Theta = -\frac{1}{2}\tan\mu(1 + 1/_6\,\phi_\Theta^2)\phi_\Theta. \tag{A.17}$$

For the arc A ($p = 1$), the arc half length (ϕ_A) and the angular speed (ω_0) are free parameters, ν_A and $\tan\mu$, and Λ_A are solved. After solving $\tan\mu$, ν_A and Λ_A are available from Eq. (A.16) and Eq. (A.17).

$$\begin{aligned}\tan\mu &= \frac{12\kappa_0\cos\alpha\phi_A}{12 + 24\kappa_0\sin\alpha\phi_A^2 + (1 + 2\kappa_0\sin\alpha)\phi_A^4 + \kappa_0\sin\alpha\phi_A^6} && \text{(A.18)}\\ &\approx \kappa_0\cos\alpha\phi_A(1 - 2\kappa_0\sin\alpha\phi_A^2 + \mathcal{O}(\phi^4)), && \text{(A.19)}\end{aligned}$$

where $\kappa_0 = k/\omega_0^2$ and Eq. (A.18) gives the exact continuity at $\phi = \phi_A$.

For the arc B ($p = -1$), ν_0 and μ are known, and ϕ_B, Λ_B, and ν_B are solved. This case is more complicated since Eqs. (A.13), (A.14), and (A.15) are non-linear in ϕ_B. To solve these equations, we assume that $\phi_A = \phi_B + \delta\phi$, expand the equations in $\delta\phi$ to solve $\delta\phi$ to read as

$$\begin{aligned}\delta\phi &= -\frac{\kappa_0\sin\alpha(48\phi_A^3 + 4\phi_A^5 + 2\phi_A^7)}{12 + 72\kappa_0\sin\alpha\phi_A^2 + (10\kappa_0\sin\alpha - 3)\phi_A^4 + 7\kappa_0\sin\alpha\phi_A^6} && \text{(A.20)}\\ &\approx -4\kappa_0\sin\alpha\phi_A^3(1 + 1/_{12}\,(1 - 24\kappa_0\sin\alpha)\phi_A^2 + \mathcal{O}(\phi^4)). && \text{(A.21)}\end{aligned}$$

Finally, the half arc length ϕ_B can be written as

$$\phi_B = \phi_A(1 - 4\kappa_0\sin\alpha\phi_A^2 + \mathcal{O}(\phi^4)). \tag{A.22}$$

Appendix B.

The definite integrals used in this study are given below. They can be deduced by partial integration, integral tables, or computer algebra systems.

$$\frac{1}{2\pi}\int_0^{2\pi}\frac{d\phi}{(1+\chi\cos\phi)^2}=\frac{1}{(1-\chi^2)^{\frac{3}{2}}} \tag{B.1}$$

$$I_0=\frac{1}{2\pi}\int_0^{2\pi}\frac{d\phi}{(1+\chi\cos\phi)^3}=\frac{(2+\chi^2)}{2(1-\chi^2)^{\frac{5}{2}}} \tag{B.2}$$

$$I_1=\frac{1}{2\pi}\int_0^{2\pi}\frac{\cos\phi d\phi}{(1+\chi\cos\phi)^3}=-\frac{3\chi}{2(1-\chi^2)^{\frac{5}{2}}} \tag{B.3}$$

$$I_2=\frac{1}{2\pi}\int_0^{2\pi}\frac{\cos^2\phi d\phi}{(1+\chi\cos\phi)^3}=\frac{(1+2\chi^2)}{2(1-\chi^2)^{\frac{5}{2}}} \tag{B.4}$$

Acknowledgements

This work was supported by Academy of Finland.

References

[1] P. Janhunen, Electric sail for spacecraft propulsion, *J. Propul. Power*, 20(4), 763–764, 2004.

[2] P. Janhunen, A. Sandroos, Simulation study of solar wind push on a charged wire: basis of solar wind electric sail propulsion, *Ann. Geophys.*, Vol. 25, 755–767, 2007.

[3] H. Seppänen, T. Rauhala, S. Kiprich, J. Ukkonen, M. Simonsson, R. Kurppa, P. Janhunen and E. Hæggström, One kilometer (1 km) electric solar wind sail tether produced automatically, *Rev. Sci. Instrum.*, Vol. 84, 095102, 2013.

[4] P. Janhunen, P. K. Toivanen, J. Polkko, S. Merikallio, P. Salminen, E. Haegström, H. Seppänen, R. Kurppa, J. Ukkonen, S. Kiprich, G. Thornell, H. Kratz, L. Richter, O. Krömer, R. Rosta, M. Noorma, J.

Envall, S. Lätt, G. Mengali, A. A. Quarta, H. Koivisto, O. Tarvainen, T. Kalvas, J. Kauppinen, A. Nuottajärvi, A. Obraztsov, Electric solar wind sail: Towards test missions, *Rev. Sci. Instrum.*, Vol. 81, 111301, 2010.

[5] ESAIL FP7 project deliverables [Retrieved on July 8, 2014] <http://www.electric-sailing.fi/fp7/fp7docs.html>.

[6] P. Janhunen, Photonic spin control for solar wind electric sail, *Acta Astronaut.*, 83, 85-90, 2013.

[7] P. Toivanen, P. Janhunen, Spin plane control and thrust vectoring of electric solar wind sail by tether potential modulation, *J. Prop. Power*, 29, 178-185, 2013.

[8] Janhunen, P., A. Quarta and G. Mengali, Electric solar wind sail mass budget model, *Geosci. Instrum. Method. Data Syst.*, 2, 85-95, 2013.

[9] P. Janunen, P. Toivanen, J. Envall, S. Merikallio, G. Montesanti, J. Gonzalez del Amo, U. Kvell, M. Noorma, S. Ltt, Overview of Electric Solar Wind Sail Applications, *Proc. Estonian Acad. Sci.*, 63, 267-278, 2014.

[10] Mengali, G. and A. Quarta, Non-Keplerian orbits for electric sails, *Cel. Mech. Dyn. Astron.*, 105, 179-195.

[11] Quarta, A.A. and G. Mengali, Electric sail mission analysis for outer solar system exploration, *J. Guid. Contr. Dyn.*, 33, 740-755, 2010.

[12] Quarta, A., G. Mengali and P. Janhunen, Electric sail for near-Earth asteroid sample return mission: case 1998 KY26, *J. Aerospace Eng.*, in press, 2014.

[13] Quarta, A.A. and G. Mengali, Electric sail missions to potentially hazardous asteroids, *Acta Astronaut.*, 66, 1506-1519, 2010.

[14] Merikallio, S. and P. Janhunen, Moving an asteroid with electric solar wind sail, *Astrophys. Space Sci. Trans.*, 6, 41-48, 2010.

[15] Toivanen, P.K. and P. Janhunen, Electric sailing under observed solar wind conditions, *Astrophys. Space Sci. Trans.*, 5, 61-69, 2009.

[16] G. Mengali, A. A. Quarta, P. Janhunen, Electric sail perfromance analysis, *J. Spacecr. Rockets*, 45, 122-129, 2008.

[17] Maxima, a Computer Algebra System [Retrieved on Oct 14, 2014], <http://maxima.sourceforge.net>.